Laser-direct-drive fusion target design with a high-Z gradient-density pusher shell

S. X. Hu [1,2,3,*] L. Ceurvorst,[1] J. L. Peebles,[1] A. Mao,[4] P. Li,[4] Y. Lu,[4] A. Shvydky,[1] V. N. Goncharov,[1,2] R. Epstein,[1]
K. A. Nichols,[1,3] R. M. N. Goshadze,[1,3] M. Ghosh,[1] J. Hinz,[1,3] V. V. Karasiev,[1] S. Zhang,[1] N. R. Shaffer,[1] D. I. Mihaylov,[1]
J. Cappelletti,[1,2] D. R. Harding,[1] C. K. Li,[5] E. M. Campbell,[6] R. C. Shah,[1] T. J. B. Collins,[1] S. P. Regan,[1,2] and C. Deeney[1]

[1]*Laboratory for Laser Energetics, University of Rochester, 250 East River Road, Rochester, New York 14623-1299, USA*
[2]*Department of Mechanical Engineering, University of Rochester, Rochester, New York 14627, USA*
[3]*Department of Physics and Astronomy, University of Rochester, Rochester, New York 14627, USA*
[4]*Department of Electrical and Computer Engineering, University of Nebraska–Lincoln, Lincoln, Nebraska 68588, USA*
[5]*Plasma Science and Fusion Center, Massachusetts Institute of Technology, Cambridge, Massachusetts 02139, USA*
[6]*MCM Consulting, San Diego, California 97127, USA*

Laser-direct-drive fusion target designs with solid deuterium-tritium (DT) fuel, a high-Z gradient-density pusher shell (GDPS), and a Au-coated foam layer have been investigated through both 1D and 2D radiation-hydrodynamic simulations. Compared with conventional low-z ablators and DT-push-on-DT targets, these GDPS targets possess certain advantages of being instability-resistant implosions that can be high adiabat ($\alpha \geqslant 8$) and low hot-spot and pusher-shell convergence (CR$_{hs} \approx 22$ and CR$_{PS} \approx 17$), and have a low implosion velocity ($v_{imp} < 3 \times 10^7$ cm/s). Using symmetric drive with laser energies of 1.9 to 2.5 MJ, 1D LILAC simulations of these GDPS implosions can result in neutron yields corresponding to $\gtrsim 50-$MJ energy, even with reduced laser absorption due to the cross-beam energy transfer (CBET) effect. Two-dimensional DRACO simulations show that these GDPS targets can still ignite and deliver neutron yields from 4 to ~ 10 MJ even if CBET is present, while traditional DT-push-on-DT targets normally fail due to the CBET-induced reduction of ablation pressure. If CBET is mitigated, these GDPS targets are expected to produce neutron yields of >20 MJ at a driven laser energy of ~ 2 MJ. The key factors behind the robust ignition and moderate energy gain of such GDPS implosions are as follows: (1) The high initial density of the high-Z pusher shell can be placed at a very high adiabat while the DT fuel is maintained at a relatively low-entropy state; therefore, such implosions can still provide enough compression $\rho R > 1$ g/cm^2 for sufficient confinement; (2) the high-Z layer significantly reduces heat-conduction loss from the hot spot since thermal conductivity scales as $\sim 1/Z$; and (3) possible radiation trapping may offer an additional advantage for reducing energy loss from such high-Z targets.

I. INTRODUCTION

After decades of perseverance, laser-driven inertial confinement fusion (ICF) has recently reached the significant milestone of realizing both burning plasma and ignition with a target gain of $G > 1$ [1–3]. This breakthrough at the National Ignition Facility (NIF) [4] has reinvigorated the prospect of commercializing fusion energy through laser-driven ICF, even though this breakthrough has only been demonstrated using the laser-indirect-drive (LID) scheme. In the LID scheme, laser energy must first be converted into thermal x rays in a gold hohlraum to indirectly drive the fusion capsule. This leads to smoother drive but lower laser-energy coupling efficiency to the imploding deuterium-tritium (DT) capsule and final hot spot, thereby resulting in only a moderate gain of $G \lesssim 10$ for the LID target design even in simulations with a reasonable amount of laser energy (~ 2 MJ). Thus, the target complexity and its limit on target gain may make the LID scheme less practical for inertial fusion energy applications and for the pursuit of significantly high neutron yields for

other high-energy density applications unless the efficiency from the electricity plug to the laser is significantly improved.

In contrast to LID, laser-direct drive (LDD) is another scheme for laser fusion [5–8] in which a millimeter-sized capsule, consisting of a thin DT ice layer covered by an ablator layer made of low-Z materials (e.g., polystyrene, beryllium, carbon, etc.) is directly irradiated by high-power laser beams. The advantage of LDD over LID is that it can couple at least twice the amount of laser energy to the imploding shell, even though other challenges exist for LDD (discussed below). In the LDD scheme, high-intensity (10^{14} to 10^{15} W/cm^2) laser irradiation on the target can heat and ablate the outer layer of the capsule, creating a large ablation pressure of $P > 50$ Mbar that subsequently drives the remaining target to implode. Given the significant acceleration in a short amount of time by laser ablation, the imploding dense DT shell can reach very high velocities ($v_{imp} > 3.7 \times 10^7$ cm/s) and attain tens of kilojoules of kinetic energy. Once such an energetic DT shell stagnates against the DT gas core, it converts part of its kinetic energy into the thermal energy of the core, forming the so-called "hot spot" by means of PdV work and the ablation of the inner side of the DT shell. The remaining kinetic energy is used to compress the dense DT layer to the high densities

*shu@lle.rochester.edu

needed for inertial confinement. In such conventional LDD target designs [9–15], all the low-Z ablator materials are ablated away before the capsule stagnates. Therefore, during the stagnation stage, the dense DT shell is pushing on the hot DT core. This type of DT-push-on-DT target requires carefully timed shocks to maintain the in-flight shell on a low-adiabat state ($\alpha = P/P_F \leqslant \sim 3$, with P being the pressure of the shell and P_F being the Fermi-degeneracy pressure of the corresponding electron density). These implosions also require a high hot-spot convergence ($CR_{hs} > 25$) and a high implosion velocity ($v_{imp} 3.7 \times 10^7$ cm/s) to reach ignition and a target gain of $G > 1$.

These stringent requirements impose great challenges on LDD fusion using conventional DT-push-on-DT target designs despite the significant milestones and progress made over the past decade [16–20]. The most daunting task in LDD is to maintain the in-flight dense DT shell at a low-entropy state for the needed compression ρR during stagnation in order to provide ample confinement time and a large burn fraction [$f_b = \rho R/(\rho R + 7)$, with ρR in units of g/cm^2] for ignition and energy gain. Low-adiabat implosions, however, are susceptible to Rayleigh-Taylor (RT) instabilities seeded by perturbations such as laser imprint [21–27], defects [28], and other nonuniformity (such as fill tube)-induced mixing [29,30]. Over the past three decades, many ideas have been proposed to overcome these challenges by decoupling the assembly of the dense DT shell from the hot-spot formation. For example, fast ignition [31–33] separates the low-velocity DT fuel assembly from an additional fast heating to spark the burn, while shock ignition [34–37] relies on a very strong shock ($P > 300$ Mbar) to initiate the burn. Similarly, other ideas such as shock-augmented ignition [38], double-shell targets [39–43], and multiple-shell targets [44,45] have also been recently explored. Specifically, in the double- and multiple-shell targets for volumetric ignition, a high-Z layer (inner shell) is used to serve as the high-density pusher to compress the liquid DT core and to provide the high $\rho R (> 1$ g/cm^2) for confinement. Although 1D designs of these volume-burn targets with high-Z layers are promising, they struggle to reach a target gain of $G > 1$ in 2D and 3D simulations, even though burning plasmas are possible with the direct-drive double-shell design [43]. These studies have shown that the high-Z layer in such targets helps reduce heat-conduction loss and to partially "recycle" or "trap" the radiation loss from the DT fuel. These benefits enable α-particle bootstrap heating in double- and multiple-shell targets to occur at a relatively low ion temperature ($T_i \sim 3.5$ keV) instead of the ~ 5 keV required for DT-push-on-DT targets. The small convergence ($CR \leqslant 10$) of DT fuel, however, adversely limits the ignition margin and target gain for double- and multiple-shell targets.

Taking into account the benefits of the high-Z layer in double- and multiple-shell targets and disregarding the drawback of their limited convergence, MacLaren *et al.* [46] have recently proposed the concept of a pushed-single-shell (PSS) design as an alternative to the low-Z ablator targets often considered by the LID scheme. The first room-temperature PSS target implosions on the NIF, which use a graded metal shell for LID, demonstrate the desired stability, as evidenced by the high ($\sim 35\%$) yield-over-simulated measurement [47]. As previously discussed, the LDD scheme can generally

couple more laser energy to the imploding shell, even in cases where the cross-beam energy transfer (CBET) effect limits the energy absorption of narrow-band lasers. Given the advantages (higher hydroefficiency and simple targets) and disadvantages (imprinting and laser-plasma instability) of the LDD scheme, we would like to examine whether or not the high-Z gradient-density pusher-shell (GDPS) design offers a viable path toward LDD fusion ignition with a target gain of $G > 1$ using currently available narrow-band driven lasers. Studies on such unconventional high-Z pusher targets are important because typical DT-push-on-DT targets are found to have little to no margin to ignition and gain in the presence of the detrimental CBET effect in LDD. Even if CBET is mitigated by future broadband lasers [48], high-Z GDPS targets could potentially provide another robust platform for high-yield applications.

In this paper, we report our studies on GDPS target-design physics based on both 1D and 2D radiation-hydrodynamic simulations. Similar to the case of direct-drive, double-shell design [43], we consider the gradient-density shell of tungsten-beryllium (W-Be) mixture by the magnetron sputtering technique [49] developed at General Atomics. The same magnetron sputtering technique has recently been used to produce the gradient-density Cr-Be shell of PSS targets for LID implosion experiments on NIF [47]. To mitigate laser-imprinting effects in LDD, we adopt a Au-coating foam layer that can be manufactured the two-photon polymerization (TPP) technique [50–53] with C-H-O-N (CHON) resin. Overall, our results show that with a certain amount of laser energy (1.9 to 2.5 MJ) under symmetric direct drive, these high-adiabat, low-convergence, and low-velocity GDPS targets can provide ~ 50-MJ neutron yield in 1D modeling, even with CBET present. Additionally, 2D simulations with laser perturbations and ice roughness indicate that these targets can still reach ignition with moderate gain (up to ~ 10-MJ neutron yield). We explore the physics behind the improved target performance of GDPS implosions over conventional DT-push-on-DT targets. Finally, we investigate the GDPS target implosions for the case of no CBET (e.g., using future broadband lasers), which produce neutron yields up to ~ 20 MJ.

The paper is organized as follows: in Sec. II, we outline general considerations for designing high-Z GDPS targets for LDD fusion. The 1D simulation results in LILAC [54] are presented in Sec. III, where we discuss the high-adiabat benefit of the high-Z pusher shell against the usual RT growth, which is key for a stable GDPS implosion. Two-dimensional radiation-hydrodynamic simulations of these GDPS target implosions using DRACO [55] are discussed in Sec. IV, in which laser perturbations, beam geometry, and DT ice roughness are considered. The role of the Au-coated foam layer to mitigate laser perturbations is another crucial factor making such LDD implosions less susceptible to laser imprint. Finally, we summarize the physics findings of GDPS target designs for LDD fusion in Sec. V.

II. GENERAL CONSIDERATIONS FOR DESIGNING GDPS TARGETS FOR LDD FUSION

As demonstrated by the direct-drive, double-shell design [43] and the recent PSS target implosion on the NIF [47], the

TABLE I. Composition and mass for each part of typical gradient-density high-Z pusher-shell target design.

	Materials	ρ (g/cm^3)	R_{start} (μm)	R_{end} (μm)	Mass (mg)
Core	DT (gas)	0.000 64	0	1627	0.012
DT layer	DT ice	0.25	1627	1672	0.385
Pusher shell	W-Be mixture	2.2 to 10.0	1672	1682	0.482
Be layer	Be	1.84	1682	1700	1.190
Foam layer	CHON	0.08	1700	1900	0.652
Solid CHON	CHON	1.20	1900	1901	0.054
Au coating	Au	19.3	1901	1901.05	0.044

use of a gradient-density shell of high-Z materials is essential to reduce the RT growth between the ablator layer and the pusher shell. Studies on how density gradient can make an ICF implosion stable have been documented in literature [56,57]. Similar to our choice for direct-drive, double-shell targets [43], we take the W-Be mixture as the pusher shell material, which can be made by the magnetron sputtering technique [49]. It has been demonstrated in target fabrication that one can continuously vary the atomic fraction of tungsten from 0 to 100% in the W-Be mixture. Specifically, we consider a range of W fractions from 0 to 31%, corresponding to the mass densities of W-Be mixtures varying from $\rho = 1.84$ g/cm^3 (pure Be) to $\rho = 9.98$ g/cm^3 (W$_{0.31}$Be$_{0.69}$). Instead of continuously varying the W fraction, the 10- to 12-μm-thick W-Be pusher shell is composed of 12 discrete W fraction steps that are practical in radiation-hydrodynamic simulations. In addition to the W-Be pusher layer, an 18- to 22-μm pure layer of Be serves as the main part of the LDD ablator. We chose Be as the main ablator material because it provides better hydroefficiency due to its high value of $\langle A \rangle / \langle Z \rangle = 2.25$, as evidenced in previous experiments [58–60].

To mitigate laser-imprinting effects [61–70] for LDD fusion, we employed a 200-μm-thick, low-density ($\rho = 80$ mg/cm^2) foam layer, which can be made by 3D printing using the TPP technique with CHON resin [50–53]. Using low-density foams to reduce laser imprints has been extensively studied in both simulations and experiments [71–74]. Recent experimental results at the Omega Laser Facility indeed show a significant reduction, particularly when the foam layer is coated with a thin ($\sim$500$-$Å) gold layer [75–77]. To make the Au coating possible, a 1-μm solid CHON layer is 3D printed on top of the foam layer. Both the foam and the solid layer can be 3D printed simultaneously using the TPP technique [50–53]. The 3D-printed foam layer with the Au coating can be made with two semishells that can be assembled over the W-Be pusher shell. Illuminated by a weak laser picket, the thin Au layer produces an $\sim$100-ps soft x-ray flash, which can melt the 3D foam structures and create low-density, overcritical plasmas to prevent direct laser imprints on the solid Be surface. This mechanism is different from the hybrid scheme for laser-imprint reduction in recent planar experiments [78] in which the first shock is produced by laser-generated soft x rays.

Finally, a 40- to 50-μm-thick cryogenic solid DT ice ($\rho = 0.25$ g/cm^3) layer in the back side of the pusher shell serves as the fusion fuel. The core is filled with DT gas at its equilibrium density of $\rho \approx 0.64$ mg/cm^3, which is also part

of the total fuel mass. We provide the material composition, density, mass, and their radial locations in Table I for a typical GDPS target design. It is evident that the W-Be pusher shell has a similar mass as to that of DT fuel. The pusher material, however, is not fusible; it only provides the needed "piston" to do the PdV work to the DT fuel. Compared to the conventional DT-push-on-DT targets, the use of a high-density, nonfusible pusher shell is an unavoidable sacrifice. The inset in Fig. 1 shows such GDPS targets (diameter of $\phi \approx 3.8$ mm), where the on-target laser intensity is plotted as a function of time. Overall, we limit the peak laser intensity to $\sim$6 $\times$ 10^{14} W/cm^2 to reduce the potential hot-electron preheat through the two-plasmon decay and stimulated Raman-scattering processes [79–82], even though the high-Z pusher layer can potentially tolerate more electron preheat than DT. It is noted that the first weak laser picket, shown in Fig. 1, is applied to generate a soft x-ray flash by the Au coating in order to melt the 3D foam structure. This goal has been preliminarily demonstrated in our most recent planar experiments [77]. The $\sim$3-ns temporal gap between the first weak picket and the main laser picket allows the melted foam structures to homogenize before the first shock is launched. The main pulse consists of a midintensity step pulse in which
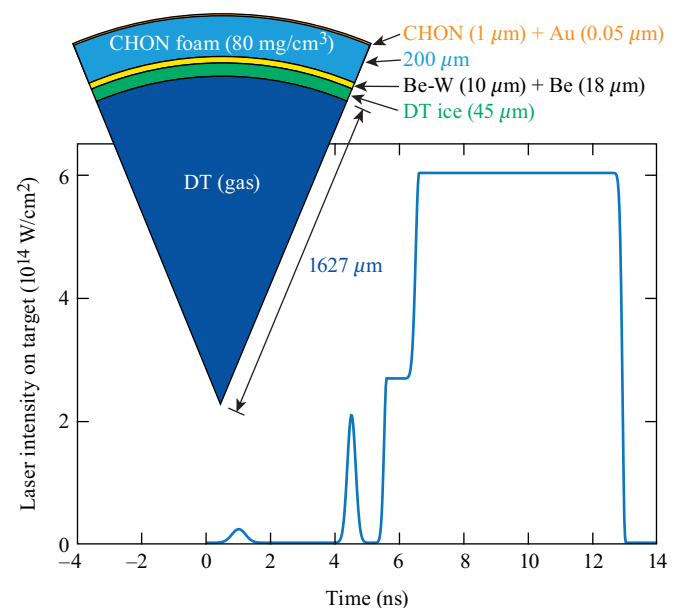
FIG. 1. High-adiabat, low-convergence laser pulse shape for laser-direct-drive, high-Z, GDPS targets. Inset: target dimensions.
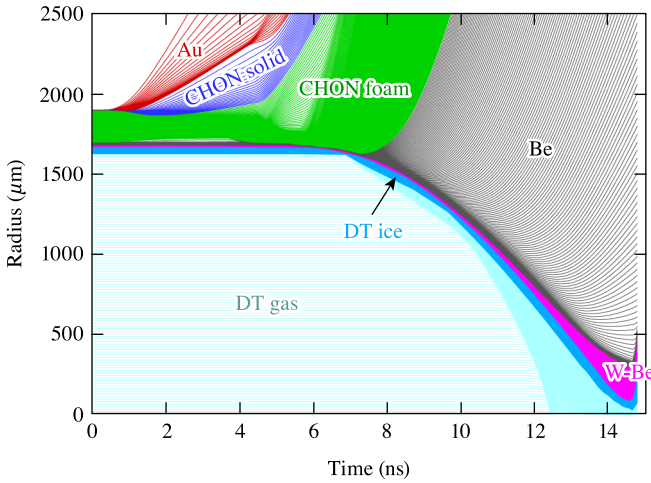
FIG. 2. Lagrangian layer position (radial) as function of time showing complete dynamics of laser-direct-drive high-*Z* GDPS implosion predicted by LILAC with state-of-the art models of nonlocal thermal transport, CBET, and FPEOS.

we intentionally put the pusher shell at a very high adiabat ($\alpha = 6$ to 10) using three shocks to mitigate the RT instability (discussed below). The total laser energy for this pulse shape is ∼1.9 MJ, even though some of our design studies explore higher driven laser energies of up to ∼2.5 MJ. It is noted that this range of laser energies is within the current–future capability of the NIF.

III. ONE-DIMENSIONAL LILAC SIMULATIONS OF GDPS TARGET IMPLOSIONS

With the GDPS target and laser pulse shape discussed above, we performed a 1D radiation-hydrodynamic simulation of its implosion by using the 1D Lagrangian code LILAC [54] (developed for LDD at the Laboratory for Laser Energetics). State-of-the-art physics models imple-

mented in our radiation-hydrodynamic simulations include the first-principles equation-of-state (FPEOS) tables for of DT [83–85], Be [86], and CHON [87], while W-Be mixtures are modeled by mixing the Be FPEOS with SESAME-EOS for W and Au by the SESAME table [88]. For thermal transport, the improved Schurtz-Nicolaï-Busquet (iSNB) nonlocal model [89] is used; for radiation transport, the 48-group diffusion model with first-principles opacity table [90] is used for DT, the astrophysics opacity table [91] is used for Be, and the averaged ion-based nonlocal thermodynamic equilibrium opacity tables [92] are used for the mid-*Z* (high-*Z*) materials of W-Be, CHON, and Au. Finally, the inverse-bremsstrahlung laser absorption also invokes the experiment-benchmarked and ray-based stimulated Brillouin-scattering model to simulate the CBET effect [93,94]. To partially reduce the CBET effect, we have optimized the ratio of laser-beam size to the target size, $R_{beam}/R_{target} = 0.8$, resulting in a total laser absorption of ∼80%.

The LILAC simulation results are presented in Figs. 2–4 for the GDPS target design shown in Fig. 1. In Fig. 2, the Lagrangian layer (radial) positions are plotted as a function of time. Figure 2 indicates that the first small laser picket "burns" off the 1-μm solid CHON and the 50-nm Au coating, with a weak shock (∼1 Mbar) crushing through the CHON foam layer before the main picket starts at $t = 4$ ns. Such preplasmas are therefore formed to help smooth laser perturbations. When the main laser picket interacts with the target, it launches a strong shock (∼20 Mbar) into the homogenized CHON foam at $R \approx 1850$ μm, which is ∼150 μm from the solid Be surface. This prevents direct laser perturbations from being imprinted onto the solid target surface and provides a certain distance for the potential healing of the shock modulation as it propagates upward in the gradient-density plasmas. Figure 2 shows that once the CHON foam is ablated away at ∼7.5 ns, the Be layer starts to serve as the high-hydroefficiency ablator. The efficient ablation drives the remaining target, consisting of the W-Be pusher
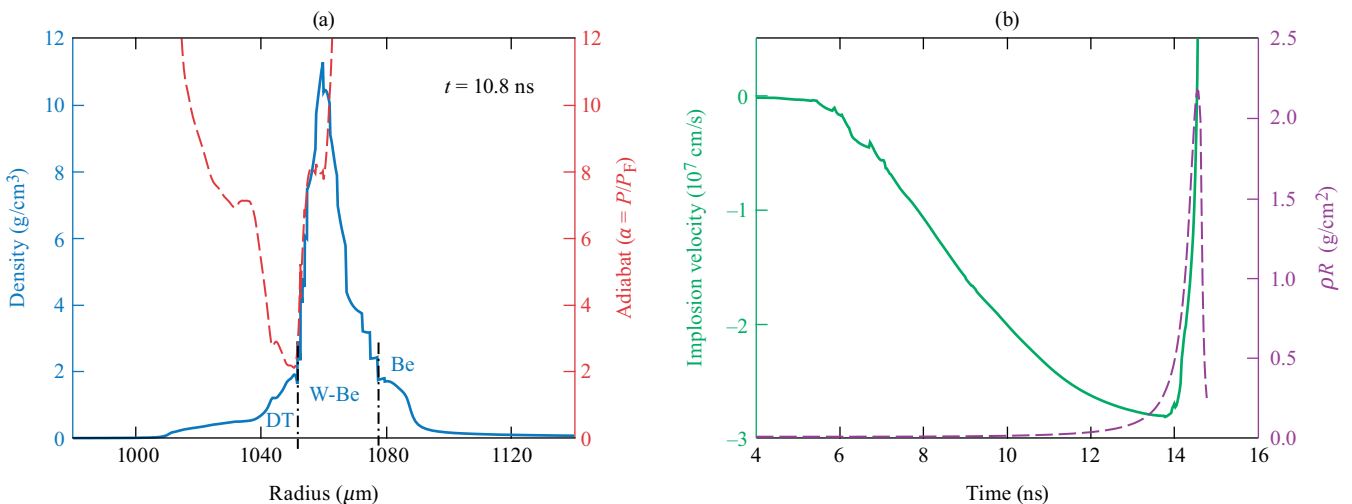
FIG. 3. (a) LILAC-predicted profiles of density (blue solid curve) and adiabat (red dashed curve) as function of target radius at $t = 10.8$ ns when shell converges to roughly two-thirds of its initial radius. (b) LILAC-predicted implosion velocity and compression areal density ρR are plotted as function of time.
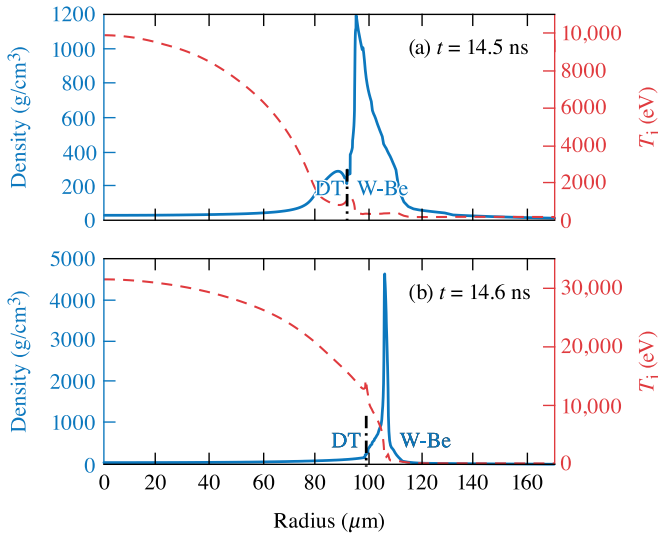
FIG. 4. LILAC-predicted profiles of density (blue solid curve) and ion temperature (red dashed curve) vs radius at (a) stagnation time ($t = 14.5$ ns) and (b) time of peak neutron production ($t = 14.6$ ns), respectively.

shell and the DT layer, to implode for the rest of ~7 ns. The W-Be shell pushing on the DT layer stagnates at $t \approx 14.5$ ns, followed by ignition and burn.

To further explore this type of GDPS target implosion, we plot the in-flight shell profiles of density (blue solid line) and adiabat (red dashed line) as a function of radius in Fig. 3(a) at $t = 10.8$ ns, when the shell converges to roughly two-thirds of its initial radius. A unique feature of this type of LDD target is that the high-density W-Be pusher shell can be placed at a very high adiabat ($\alpha \approx 8$), while the main DT mass can remain at a low-entropy state ($\alpha \approx 2$ to 3). The reason that one can keep the pusher shell on high adiabat is due to the fact that high-Z materials are electron rich so that shock compression can easily bring them to high-entropy states. This has also been discussed in double-shell design papers [42,43]. Figure 3(a) shows that the estimated percentage of the DT mass at low adiabat ($\alpha \leqslant 3$) is about ~68% of the total DT mass. In addition, the Be ablator layer is set at an extremely high adiabat ($\alpha \approx 50$), which is beyond the plotting range of Fig. 3(a). This feature is very important because it allows the GDPS implosion to be less susceptible to the RT instability since a higher adiabat at ablation front generally favors the ablative stabilization of RT growth [95–97]. DRACO simulations (discussed in the next section) demonstrate the benefit of such an extreme adiabatic "shaping." Figure 3(b) shows the implosion velocity versus time, as well as the areal density (ρR) history. It indicates that this type of GDPS target requires only a relatively low-implosion velocity of $v_{\text{imp}} \approx 281$ km/s to reach ignition, which is ~30% lower than the convention DT-push-on-DT target, which requires a minimum implosion of $v_{\text{imp}} \approx 370$ km/s. The lower-implosion velocity needed for GDPS targets can also relax the shell acceleration for a smaller RT growth rate. The reason GDPS targets require a lower-implosion velocity to ignite is due to their high initial density (e.g., $\rho_0 \approx 10$ g/cm^3 for the case discussed here), which is much greater than a typical DT-push-on-DT target. Further-

TABLE II. Summary of 1D target performance for laser-direct-drive fusion target using high-Z GDPS design, with driven laser energy of ~1.9 MJ with and without CBET. All quantities in bracket "$\langle \ldots \rangle$" are neutron averaged.

Target performance	With CBET	Without CBET
Neutron yield	2.08×10^{19} (~58 MJ)	2.25×10^{19} (~63 MJ)
v_{imp}	~281 km/s	~310 km/s
$\text{CR}_{\text{hs}}/\text{CR}_{\text{PS}}$	~21.7/~17	~22/~17.5
$\langle \rho R \rangle_{\text{DT}}$	0.644 g/cm^2	0.744 g/cm^2
$\langle \rho R \rangle_{\text{shell}}$	1.11 g/cm^2	1.23 g/cm^2
$\langle T \rangle_{\text{i}}$	41.1 keV	49.0 keV
$\langle P \rangle$	1.85 Tbar	2.74 Tbar

more, the ignition-relevant kinetic energy ($K > 50$ kJ) of the in-flight shell, $\sim \rho v_{\text{imp}}^2$, can be attained with a relatively lower velocity for high-density GDPS targets. At stagnation, such a slow GDPS implosion can still produce a very high total compression $\rho R \approx 2$ g/cm^2, as shown by the dashed curve in Fig. 3(b). The LILAC-predicted areal density of DT fuel (including the hot spot and DT shell) can extend over ~600 mg/cm^2, even for simulations with CBET.

Finally, Fig. 4 illustrates the density and ion-temperature conditions of the GDPS implosion during the stages of stagnation [Fig. 4(a)] and peak neutron production [Fig. 4(b)]. It is evident that during stagnation, the W-Be shell pushes the DT layer against the hot-spot DT core. This compresses the DT layer to a relatively high density ($\rho \approx 300$ g/cm^3) and causes PdV work to heat the DT core to a peak ion temperature of $T_{\text{i}} \approx 10$ keV. The resulting hot spot, with a large core radius of $R_{\text{hs}} \approx 75$ μm, is dense ($\rho \approx 40$ g/cm^3) and hot enough to generate bootstrap heating by its DT fusion-produced alpha particles. Figure 4(b) shows that the initiated burn wave depletes the compressed DT shell, rendering the entire DT fuel into a burning hot core, which reaches a high temperature of $T_{\text{i}} \approx 30$ keV, still being confined by the W-Be pusher shell. An enormous amount of pressure ($P \approx 200$ Gbar) is produced, which launches an extremely strong shock that compresses the W-Be pusher layer to densities over ~4000 g/cm^3. The large pusher shell ρR (~1.1 g/cm^2) provides ample confinement time (~100 ps) for the DT core to burn, generating a high neutron yield of $Y \approx 2.08 \times 10^{19}$ (corresponding to ~58-MJ energy) from the 1D LILAC simulation. Table II summarizes the overall performance of the GDPS target from the LILAC prediction. In contrast to the conventional DT-push-on-DT targets, these GDPS targets ignite at relatively lower hot-spot convergence ratios of $\text{CR}_{\text{hs}} \sim 22$, while the pusher shell needs only a convergence ratio of $\text{CR}_{\text{PS}} \sim 17$. In addition, the LILAC simulation without CBET for the same GDPS target is also included in Table II for comparison. Overall, the no-CBET case does somewhat better than the CBET case; in particular, the implosion velocity can be increased by ~10%, which provides more margin for ignition and gain in 2D simulations (discussed below). For ICF to be successful, implosion velocity and stability need always to be balanced. As long as certain shell acceleration does not cause the imploding shell to fall apart, higher implosion velocity can always help to reach ignition favorably.

TABLE III. Summary of 1D target performance for laser-direct-drive fusion target using high-Z GDPS design and driven laser energy of $\sim$2.5 MJ with and without CBET. All quantities in bracket $\langle\dots\rangle$ are neutron averaged.

Target performance	With CBET	Without CBET
Neutron yield	1.81×10^{19} ($\sim$51 MJ)	2.06×10^{19} ($\sim$58 MJ)
v_{imp}	$\sim$292 km/s	$\sim$336 km/s
CR_{hs}/CR_{PS}	$\sim$22.0/$\sim$16.3	$\sim$21.8/$\sim$16.6
$\langle\rho R\rangle_{DT}$	0.579 g/cm^2	0.673 g/cm^2
$\langle\rho R\rangle_{shell}$	1.11 g/cm^2	1.34 g/cm^2
$\langle T\rangle_i$	38.3 keV	50.6 keV
$\langle P\rangle$	1.56 Tbar	2.87 Tbar

In addition to the 1.9-MJ design, we also explore possible outcomes when using a slightly higher driven laser energy. To this end, we examined a similar target design with 2.5-MJ laser energy. The target size and composition are very similar to those of the 1.9-MJ target discussed above, except that the W-Be pusher layer is slightly thicker (changing from 10 to 12 μm); the thickness of Be ablator layer is increased by 4 to 22 μm (i.e., the Be-layer thickness changes from 18 μm in the 1.9-MJ case to 22 μm for the 2.5-MJ case); and the DT-ice layer is reduced from 45- to 40 μm thick. In addition, the laser pulse is extended to a total pulse duration of 13.5 ns. The LILAC predictions of this GDPS targets are summarized in Table III. Overall, we saw similar 1D performance as that of the 1.9-MJ target, while the 2D DRACO simulations of this 2.5-MJ target show more margin for ignition and gain (discussed in the next section). The LILAC difference between 2.5- and 1.9-MJ cases was caused by the $\sim$10% difference of $\langle\rho R\rangle_{DT}$ (see Tables II and III). The 10% lower $\langle\rho R\rangle_{DT}$ in the 2.5-MJ case (smaller DT-ice thickness) gives less neutron yield, even though its implosion velocity is slightly higher. In the 2D case to be discussed in Sec. IV, the $\langle\rho R\rangle_{DT}$ difference is masked by perturbations. Instead, the slightly higher velocity for the 2.5-MJ case gives more hot-spot energy density leading to more neutron yield.

IV. TWO-DIMENSIONAL DRACO SIMULATION RESULTS

Given the promising 1D target designs discussed above, we now examine if such GDPS targets are able to survive the nominal laser and target perturbations in 2D radiation-hydrodynamic simulations. For this purpose, we have performed DRACO simulations of GDPS target implosions, including perturbations from laser port geometry (taking the 60-beam OMEGA configuration as an example), laser-imprint modes up to $\ell_{max} = 100$, and the long-wavelength roughness of $\sigma_{rms} = 1$ μm at the rear surface of DT-ice layer. Each laser beam has a super-Gaussian (SG-5) spatial shape that covers only 80% of the target diameter. To demonstrate the least-favorable outcome, we turned off the smoothing by spectral dispersion. The target is discretized on a 2D grid of 650×350 zones on the cylindrical r–z plane while the symmetry axis is around the z axis. Three-dimensional ray tracing [94] is applied to model the laser deposition with the choice of whether or not to invoke CBET. The same state-of-the-art physics

models used in LILAC are also employed in these DRACO simulations, which use a Lagrangian mode with rezoning. These results are presented in Figs. 5–8 for the case using 1.9-MJ laser energy. It is noted that these 2D simulations are done for a *hypothetical* direct-drive laser which has the 60-beam OMEGA port geometry but NIF-scale laser energy. For a symmetrical and direct-drive laser facility in the future, it is expected that the number of beams can be significantly larger than 60, which could provide more beam overlap on target so as to reduce perturbations induced by port geometry.

Figures 5(a)–5(c) show the density contours during the acceleration stage of the GDPS target implosion at times of $t = 11$, 12, and 13 ns with CBET present. It is evident that the density of the pusher shell is perturbed as the implosion proceeds, which is caused by the usual RT instability growth of laser and target perturbations. Since the in-flight pusher shell is at a very high adiabat [$\alpha \approx 8$; see Fig. 3(a)], the RT growth is moderate; therefore, the shell does not break up, as shown in Fig. 5(c). Figures 5(d)–5(f) illustrate situations at the corresponding times in the case without CBET, which provides greater laser absorption that drives the shell to move $\sim$10% faster than in the CBET simulation. As a consequence, Figs. 5(d)–5(f) indicate that the target converges to a smaller radius at the same corresponding times and that the perturbations grow due to the larger acceleration. This is further evident in Fig. 6, where the root-mean-square (σrms) of the areal-density (ρR) modulation of the imploding target is plotted as a function of time. The slope of $\sigma_{rms}(\rho R)$ is larger for the no-CBET case. At the end of acceleration ($t = 13$ ns), the no-CBET simulation produces double the modulation of shell's areal density: $\sigma_{rms}(\rho R) \approx 16$ mg/cm^2 (no-CBET) versus $\sigma_{rms}(\rho R) \approx 8$ mg/cm^2 (CBET). The corresponding areal densities are $\rho R = 121$ mg/cm^2 (no-CBET) and $\rho R = 87$ mg/cm^2 (CBET) at this time, respectively.

After the laser pulse ends at $t = 13$ ns, the imploding shell coasts inward with spherical convergence. Once the return shock from the hot spot reaches the dense shell, the target starts to decelerate. Two density-contour plots in Fig. 7 show the deceleration phase of the two GDPS implosion simulations with and without CBET. Instead of plotting them at the same time, we illustrate the differences between the simulations as the shell converges to the similar radius. As shown in Fig. 7, the shell moves faster by 350 to 400 ps in the no-CBET simulation as compared to the CBET case. The strong RT growth during the deceleration phase of the final $\sim$500 ps before stagnation is evident by the steep increase of $\sigma_{rms}(\rho R)$ shown in Fig. 6 (before its peak). Consequently, density "spikes" from the pusher shell develop, which push on both the dense DT and the hot spot [see Figs. 7(b) and 7(d)]. Fortunately, this deceleration-phase RT growth does not completely quench the ignition (burn) in the hot spot. As shown in Figs. 8(a) and 8(b), the contours of the density (upper) and ion temperature (lower) are plotted at the start of the burn-wave propagation for the cases with and without CBET, respectively. The results show that despite the significant deceleration-phase RT growth, the hot spot is dense and hot enough to initiate the burn, even when CBET is present in the DRACO simulation. As expected, the ion temperature of $T_i \approx 20$ keV in Fig. 8(b) is higher in the no-CBET simulation due to its $\sim$10% higher implosion velocity of $\sim$310 km/s
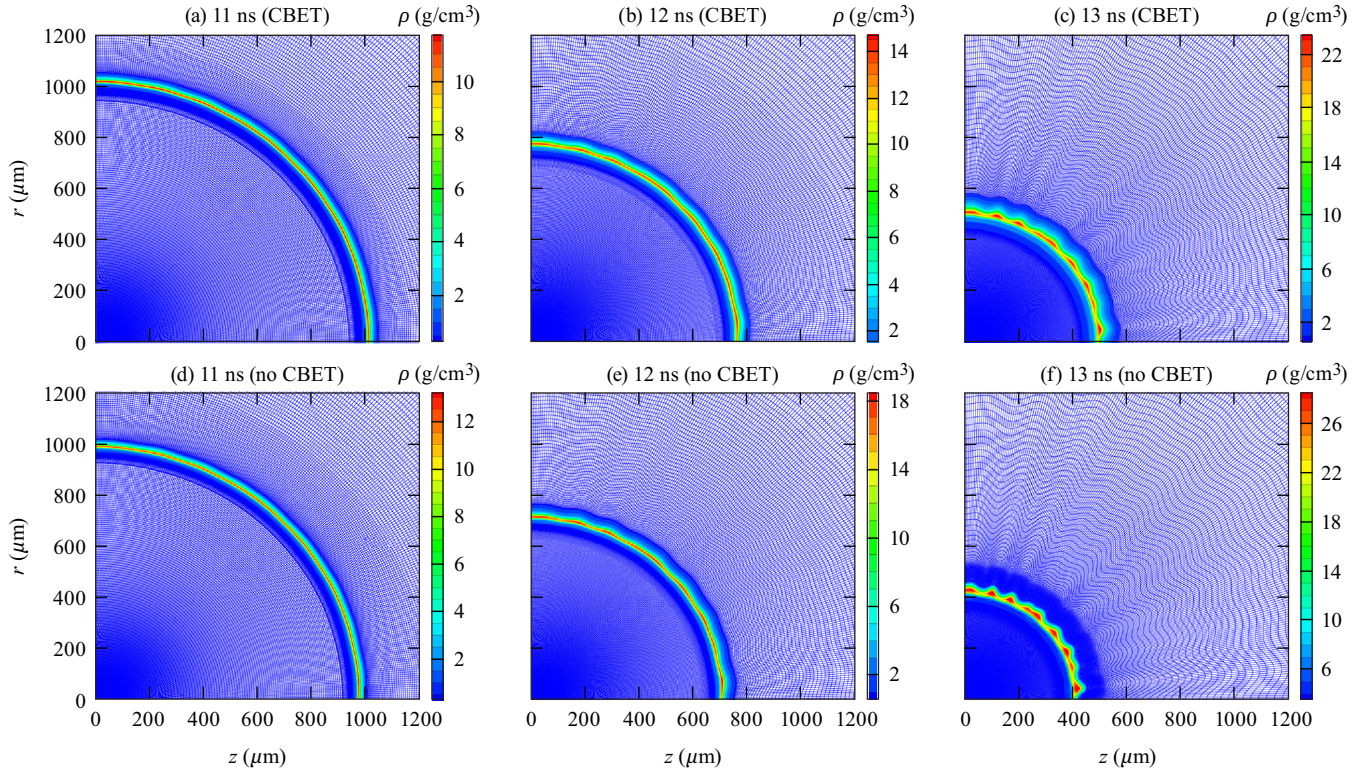
FIG. 5. Density contour plots on (r–z) plane from 2D DRACO simulations of high-Z GDPS implosion during acceleration phase at different times of (a) $t = 11$ ns, (b) $t = 12$ ns, and (c) $t = 13$ ns for simulations with CBET. [(d)–(f)] Another DRACO simulation of same target without CBET.

(versus $\sim$281 km/s with CBET). Figure 8 also indicates that for GDPS targets, there is a relatively large and clean volume of DT fuel ($\phi \approx 120$ μm) for the burn to sustain, even though the large deceleration-phase RT growth is unavoidable. The high-Z layer confines the heat and sustains the burn for $\sim$100 ps. Finally, a significant amount of the dense DT layer is burned off, which leads to moderate neutron production and energy gain.

The target performance predicted by the two DRACO simulations (with and without CBET) are summarized in Table IV.
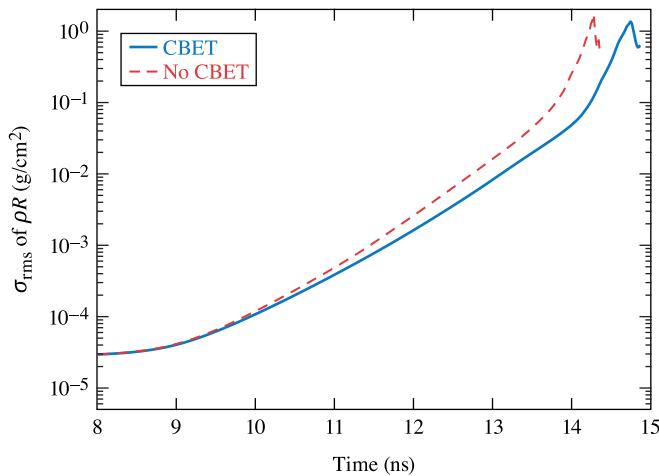
FIG. 6. Root-mean-square (σrms) of areal-density (ρR) modulation of the imploding target as function of time, with and without CBET in DRACO simulations.

Compared to the 1D performance, the nominal laser and target perturbations invoked in DRACO simulations degrade the GDPS implosions from their 1D predictions. In particular, these perturbations have reduced the ion temperatures from the LILAC-predicted values of 40 to 50 keV down to only 10 to 15 keV. Three effects contribute to the observed ion-temperature reduction: (1) the density-perturbed pusher shell does not convert its full kinetic energy to the thermal energy of the hot spot; instead, some kinetic energy is partitioned into the unwanted residual motion of the DT fuel; (2) the perturbations increase the surface area between hot DT fuel and the cold high-Z pusher while the cold spikes of the high-Z pusher cool the DT temperature; and (3) the confinement time is effectively reduced due to the rapid expansion of the low-density portion ("bubbles") of the pusher shell. Nevertheless, these targets can still produce 4- to 10-MJ neutron yield in these DRACO runs. Additional optimizations—for

TABLE IV. Summary of 2D DRACO simulation results for $\sim$1.9-MJ high-Z GDPS target with and without CBET. All quantities in bracket $\langle \ldots \rangle$ are neutron averaged.

Target performance	With CBET	Without CBET
Neutron yield	1.41×10^{18} ($\sim$4 MJ)	3.28×10^{18} ($\sim$9.2 MJ)
$\langle \rho R \rangle_{DT}$	0.624 g/cm^2	0.704 g/cm^2
$\langle \rho R \rangle_{shell}$	0.97 g/cm^2	1.12 g/cm^2
$\langle T \rangle_i$	10.7 keV	15.1 keV
$\langle$Burn volume$\rangle$	2.47×10^4 μm^3	2.39×10^4 μm^3
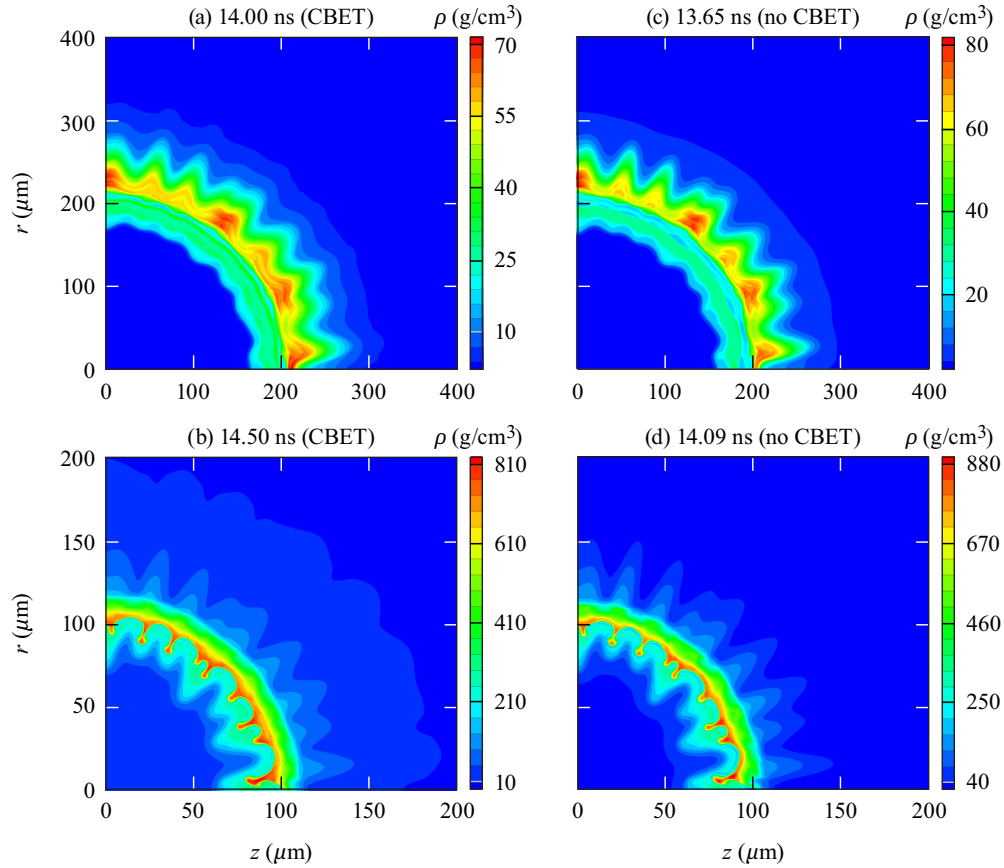
FIG. 7. Density contour plots on (*r*–*z*) plane from 2D DRACO simulations of high-Z GDPS implosion during deceleration phase: [(a),(c)] with and [(b),(d)] without CBET.

example, increasing the density-gradient scale length of the pusher shell in the DT-pusher interface—will help to reduce the deceleration of RT growth for enhancing the GDPS target performance.

Finally, DRACO simulations for the GDPS target design with 2.5-MJ driven laser energy (Table III) are shown in Fig. 9. Similar to Fig. 8, density and ion-temperature contour plots are shown for both CBET and no-CBET cases, respectively, in Figs. 9(a) and 9(b) as the burn wave starts

to propagate. In comparison to the 1.9-MJ case, the ion temperatures are generally higher for the 2.5-MJ drive due to the availability of more kinetic energy for the hot-spot assembly. The stronger bootstrap heating increases the neutron-averaged ion temperatures to 14–18 keV, leading to a greater neutron yield. As summarized in Table V, DRACO simulations predict output energies in the range of 10.5 to 17.7 MJ, producing a higher margin than the 1.9-MJ target. Overall, we find that GDPS targets are robust to ignition in the direct-drive scheme.
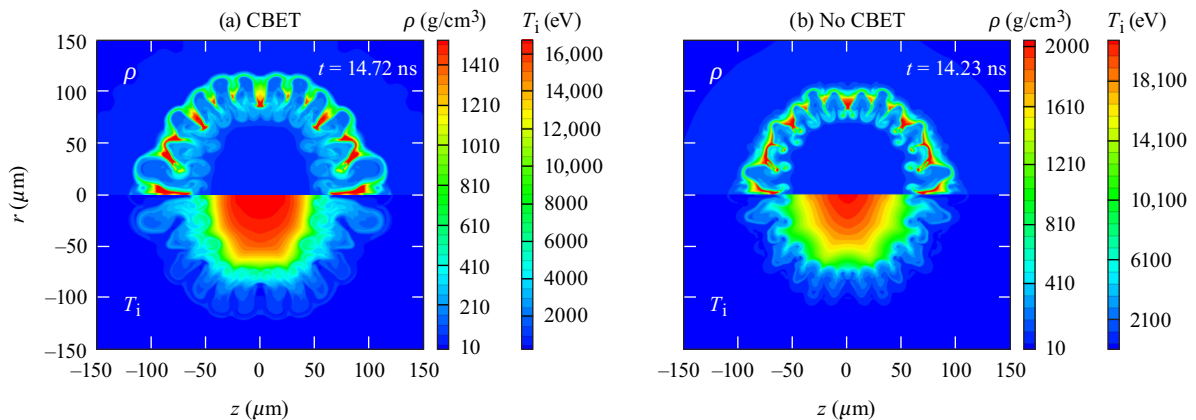
FIG. 8. Density (ρ) and ion-temperature (T_i) contour plots on (*r*–*z*) plane at DT-plasma burning stage: (a) with CBET at $t = 14.72$ ns and (b) without CBET at $t = 14.23$ ns for high-Z GDPS target with driven laser energy of ~1.9 MJ.
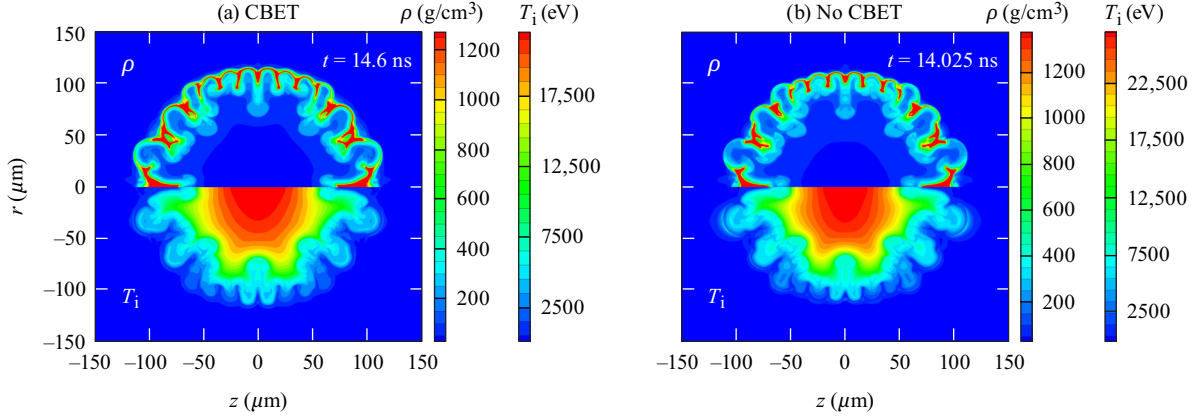
FIG. 9. Density (ρ) and ion-temperature (T_i) contour plots on (r–z) plane at DT-plasma burning stage: (a) with CBET at t = 14.6 ns and (b) without CBET at t = 14.025 ns, for slightly different high-Z GDPS target with driven laser energy of $\sim$2.5 MJ.

In the meantime, there are opportunities optimizing this type of GDPS target toward high gain. Optimizing the ratio of the DT mass to the pusher-shell mass, for instance, is an area that could be further explored in future studies.

The high-Z GDPS target designs discussed in this paper have considered a hypothetical NIF-scale laser with symmetric direct drive, which does not exist at the moment. However, given the prospect of inertial fusion energy being actively pursued around the world, symmetric direct-drive laser facilities having energies of $\sim$1–3 MJ are expected to become a reality in the next decade or two. The other pathway is to modify the indirect-drive geometry of NIF and/or LMJ to symmetric drive. Regardless of the path forward, our current plan is to scale down these high-Z GDPS designs to OMEGA-size targets for experimental tests at the Omega Laser Facility, in which $\sim$27-kJ lasers can symmetrically illuminate targets for spherical implosions. We hope these small-scale GDPS experiments can provide the necessary benchmarks to our radiation-hydrodynamic simulations, which shall position us towards demonstrating the potential of such high-Z GDPS targets on large-scale and direct-drive laser facilities in the near future.

V. SUMMARY

In summary, we have performed LDD fusion target designs with a high-Z GDPS in 1D and 2D radiation-hydrodynamic simulations. These studies show that ignition with moderate gain is feasible with these GDPS targets, even when

the CBET effect is still present. To put this in perspective, the hydroequivalent scaleup of the currently best-performed DT-push-on-DT targets on OMEGA to a *hypothetical* symmetric direct drive with NIF-scale laser energy ($\sim$2.15 MJ) cannot reach a target gain of $G > 1$ with CBET on. Instead, such DT-push-on-DT targets might give neutron yields of $Y \leqslant \sim 5.5 \times 10^{17}$ only in the so-called *burning plasma* regime [98]. Compared with the conventional DT-push-on-DT targets, the robustness of such GDPS implosions can be attributed to the following facts: (1) the high-Z pusher shell can be maintained at a very high adiabat ($\alpha = 6$ to 10) while the DT fuel is at a low-entropy state; (2) the GDPS target ignition requires a relatively lower-implosion velocity of $v_{imp} = 250$ to 300 km/s, which is $\sim$30% lower than the minimum implosion velocity ($v_{imp} = 370$ km/s) required for conventional DT-push-on-DT targets; (3) GDPS implosions only require a relatively smaller convergence (CR$_{hs} \sim 22$ and CR$_{PS} \sim 17$) to ignite; and (4) the high-Z layer serves as a heat insulator to reduce thermal conduction loss, in addition to the possible radiation "recycling (trapping)" by the high-Z pusher. Two-dimensional DRACO simulations show that ignition that produces 4- to 10-MJ neutrons could be possible with a driven laser of 1.9 to 2.5 MJ in symmetric LDD configurations even with CBET present. Once CBET is mitigated in future facilities, GDPS targets have the potential for even larger margins, which can possibly give 10- to 20-MJ neutron yields for the same laser energy. Optimization through gradient-density shaping might further reduce the deceleration-phase RT growth, leading to enhanced target performance.

TABLE V. Summary of 2D DRACO simulation results for $\sim$2.5-MJ high-Z GDPS target with and without CBET. All quantities in bracket $\langle \ldots \rangle$ are neutron averaged.

Target performance	With CBET	Without CBET
Neutron yield	3.74×10^{18}	6.32×10^{18}
	($\sim$10.5 MJ)	($\sim$17.7 MJ)
$\langle \rho R \rangle_{DT}$	0.590 g/cm^2	0.646 g/cm^2
$\langle \rho R \rangle_{shell}$	1.06 g/cm^2	1.21 g/cm^2
$\langle T \rangle_i$	13.7 keV	17.5 keV
$\langle$Burn volume$\rangle$	3.94×10^4 μm^3	3.71×10^4 μm^3

usefulness of any information, apparatus, product, or process disclosed, or represents that its use would not infringe privately owned rights. Reference herein to any specific commercial product, process, or service by trade name, trademark, manufacturer, or otherwise does not necessarily constitute or imply its endorsement, recommendation, or favoring by the U.S. Government or any agency thereof. The views and opinions of authors expressed herein do not necessarily state or reflect those of the U.S. Government or any agency thereof.

[1] A. B. Zylstra *et al.*, Nature (London) **601**, 542 (2022).

[2] H. Abu-Shawareb, R. Acree, P. Adams *et al.*, Phys. Rev. Lett. **129**, 075001(2022).

[3] DOE Website, https://www.energy.gov/articles/doe-national-laboratory-makes-history-achieving-fusion-ignition; H. Abu-Shawareb *et al.*, Phys. Rev. Lett. (to be published).

[4] E. M. Campbell and W. J. Hogan, Plasma Phys. Control. Fusion **41**, B39 (1999).

[5] R. S. Craxton *et al.*, Phys. Plasmas **22**, 110501 (2015).

[6] V. N. Goncharov *et al.*, Phys. Plasmas **21**, 056315 (2014).

[7] S. E. Bodner *et al.*, Phys. Plasmas **5**, 1901 (1998).

[8] A. J. Schmitt and S. P. Obenschain, Phys. Plasmas **30**, 012702 (2023).

[9] S. E. Bodner, D. G. Colombant, A. J. Schmitt, and M. Klapisch, Phys. Plasmas **7**, 2298 (2000).

[10] B. Canaud *et al.*, Nucl. Fusion. **44**, 1118 (2004).

[11] S. Skupsky *et al.*, Phys. Plasmas **11**, 2763 (2004).

[12] V. N. Goncharov *et al.*, Phys. Rev. Lett. **104**, 165001 (2010).

[13] S. X. Hu *et al.*, Phys. Plasmas **17**, 102706 (2010).

[14] T. J. B. Collins *et al.*, Phys. Plasmas **19**, 056308 (2012).

[15] V. N. Goncharov *et al.*, Plasma Phys. Control. Fusion **59**, 014008 (2016).

[16] T. C. Sangster *et al.*, Phys. Plasmas **20**, 056317 (2013).

[17] S. P. Regan *et al.*, Phys. Rev. Lett. **117**, 025001 (2016).

[18] V. Gopalaswamy *et al.*, Nature (London) **565**, 581 (2019).

[19] A. Lees R. Betti, J.P. Knauer, V. Gopalaswamy, D. Patel, K. M. Woo, K.S. Anderson, E.M. Campbell, D. Cao, J. Carroll-Nellenback *et al.*, Phys. Rev. Lett. **127**, 105001 (2021).

[20] A. Lees *et al.*, Phys. Plasmas **30**, 012709 (2023).

[21] S. E. Bodner, Phys. Rev. Lett. **33**, 761 (1974).

[22] R. Ishizaki and K. Nishihara, Phys. Rev. Lett. **78**, 1920 (1997).

[23] R. Ishizaki and K. Nishihara, Phys. Rev. E **58**, 3744 (1998).

[24] S. P. Obenschain *et al.*, Phys. Plasmas **9**, 2234 (2002).

[25] S. Fujioka *et al.*, Phys. Rev. Lett. **92**, 195001 (2004).

[26] S. X. Hu, G. Fiksel, V. N. Goncharov, S. Skupsky, D. D. Meyerhofer, and V. A. Smalyuk, Phys. Rev. Lett. **108**, 195003 (2012).

[27] M. Karasik, J. L. Weaver, Y. Aglitskiy, J. Oh, and S. P. Obenschain, Phys. Rev. Lett. **114**, 085001 (2015).

[28] I. V. Igumenshchev *et al.*, Phys. Plasmas **20**, 082703 (2013).

[29] B. M. Haines, F. F. Grinstein, and J. R. Fincke, Phys. Rev. E **89**, 053302 (2014).

[30] B. M. Haines *et al.*, Nat. Commun. **11**, 544 (2020).

[31] M. Tabak, J. Hammer, M. E. Glinsky, W. L. Kruer, S. C. Wilks, J. Woodworth, E. M. Campbell, M. D. Perry, and R. J. Mason, Phys. Plasmas **1**, 1626 (1994).

[32] R. Kodama *et al.*, Nature (London) **418**, 933 (2002).

[33] P. A. Norreys *et al.*, Nucl. Fusion. **49**, 104023 (2009).

[34] R. Betti, C. D. Zhou, K. S. Anderson, L. J. Perkins, W. Theobald, and A. A. Solodov, Phys. Rev. Lett. **98**, 155001 (2007).

[35] W. Theobald *et al.*, Phys. Plasmas **19**, 102706 (2012); W. L. Shang *et al.*, Phys. Rev. Lett. **119**, 195001 (2017).

[36] R. H. H. Scott, C. Beaucourt, H.-P. Schlenvoigt, K. Markey, K. L. Lancaster, C. P. Ridgers, C. M. Brenner, J. Pasley, R. J. Gray, I. O. Musgrave *et al.*, Phys. Rev. Lett. **109**, 015001 (2012).

[37] R. H. H. Scott, K. Glize, L. Antonelli, M. Khan, W. Theobald, M. Wei, R. Betti, C. Stoeckl, A. G. Seaton, T. D. Arber *et al.*, Phys. Rev. Lett. **127**, 065001 (2021).

[38] R. H. H. Scott, D. Barlow, W. Trickey, A. Ruocco, K. Glize, L. Antonelli, M. Khan, and N. C. Woolsey, Phys. Rev. Lett. **129**, 195001 (2022).

[39] W. S. Varnum *et al.*, Phys. Rev. Lett. **84**, 5153 (2000).

[40] B. M. Haines *et al.*, Phys. Plasmas **28**, 032709 (2021).

[41] H. F. Robey, P. A. Amendt, J. L. Milovich, H.-S. Park, A. V. Hamza, and M. J. Bono, Phys. Rev. Lett. **103**, 145003 (2009).

[42] D. S. Montgomery *et al.*, Phys. Plasmas **25**, 092706 (2018).

[43] S. X. Hu *et al.*, Phys. Rev. E **100**, 063204 (2019).

[44] K. Molvig, M. J. Schmitt, B. J. Albright, E. S. Dodd, N. M. Hoffman, G. H. McCall, and S. D. Ramsey, Phys. Rev. Lett. **116**, 255003 (2016).

[45] B. S. Scheiner *et al.*, Phys. Plasmas **26**, 072707 (2019).

[46] S. A. MacLaren *et al.*, Phys. Plasmas **28**, 122710 (2021).

[47] E. L. Dewald *et al.*, Phys. Plasmas **29**, 052707 (2022).

[48] C. Dorrer *et al.*, Opt. Express **29**, 16135 (2021).

[49] H. Xu *et al.*, Fusion Sci. Technol. **73**, 354 (2018).

[50] O. Stein, Y. Liu, J. Streit, J. H. Campbell, Y. F. Lu, Y. Aglitskiy, and N. Petta, Fusion Sci. Technol. **73**, 153 (2018).

[51] L. J. Jiang *et al.*, Fusion Sci. Technol. **70**, 295 (2016).

[52] Y. Liu, J. H. Campbell, O. Stein, L. Jiang, J. Hund, and Y. F. Lu, Nanomaterials **8**, 498 (2018).

[53] D. R. Harding, S. Muller, M. Bonino, Y. F. Lu, P. Fan, and S. Huang, "Laser-based microfabrication and metrology of laser-driven inertial fusion targets," presented at The 21st International Symposium on Laser Precision Microfabrication (LPM 2020), Virtual, June 2020.

[54] J. Delettrez, R. Epstein, M. C. Richardson, P. A. Jaanimagi, and B. L. Henke, Phys. Rev. A **36**, 3926 (1987).

[55] P. B. Radha *et al.*, Phys. Plasmas **12**, 056307 (2005).

[56] N. Metzler, A. L. Velikovich, A. J. Schmitt, and J. H. Gardner, Phys. Plasmas **9**, 5050 (2002).

[57] N. Metzler, A. L. Velikovich, and J. H. Gardner, Phys. Plasmas **6**, 3283 (1999).

[58] D. T. Michel, V. N. Goncharov, I. V. Igumenshchev, R. Epstein, and D. H. Froula, Phys. Rev. Lett. **111**, 245005 (2013).

[59] J. L. Kline *et al.*, Phys. Plasmas **23**, 056310 (2016).

[60] A. B. Zylstra *et al.*, Phys. Plasmas **26**, 052707 (2019).

[61] V. N. Goncharov *et al.*, Phys. Plasmas **7**, 2062 (2000).

[62] H. Nishimura *et al.*, Nucl. Fusion. **40**, 547 (2000).

[63] T. R. Boehly *et al.*, Phys. Plasmas **8**, 2331 (2001).

[64] A. N. Mostovych, D. G. Colombant, M. Karasik, J. P. Knauer, A. J. Schmitt, and J. L. Weaver, Phys. Rev. Lett. **100**, 075002 (2008).

[65] T. Watari *et al.*, Phys. Plasmas **15**, 092109 (2008).

[66] V. A. Smalyuk, S. X. Hu, J. D. Hager, J. A. Delettrez, D. D. Meyerhofer, T. C. Sangster, and D. Shvarts, Phys. Rev. Lett. **103**, 105001 (2009).

[67] S. X. Hu *et al.*, Phys. Plasmas **16**, 112706 (2009).

[68] G. Fiksel, S. X. Hu, V. N. Goncharov, D. D. Meyerhofer, T. C. Sangster, V. A. Smalyuk, B. Yaakobi, M. J. Bonino, and R. Jungquist, Phys. Plasmas **19**, 062704 (2012).

[69] S. X. Hu *et al.*, Phys. Plasmas **23**, 102701 (2016).

[70] D. T. Michel, S. X. Hu, A. K. Davis, V. Yu. Glebov, V. N. Goncharov, I. V. Igumenshchev, P. B. Radha, C. Stoeckl, and D. H. Froula, Phys. Rev. E **95**, 051202(R) (2017).

[71] R. G. Watt *et al.*, Phys. Rev. Lett. **81**, 4644 (1998).

[72] S. Depierreux *et al.*, Phys. Rev. Lett. **102**, 195005 (2009).

[73] B. Delorme *et al.*, Phys. Plasmas **23**, 042701 (2016).

[74] S. X. Hu *et al.*, Phys. Plasmas **25**, 082710 (2018).

[75] R. J. Mason, R. A. Kopp, H. X. Vu, D. C. Wilson, S. R. Goldman, R. G. Watt, M. Dunne, and O. Willi, Phys. Plasmas **5**, 211 (1998).

[76] D. Batani *et al.*, Phys. Rev. E **62**, 8573 (2000).

[77] J. L. Peebles *et al.* (unpublished).

[78] L. Ceurvorst *et al.*, Phys. Rev. E **101**, 063207 (2020).

[79] D. T. Michel *et al.*, Phys. Rev. Lett. **109**, 155007 (2012).

[80] B. Yaakobi *et al.*, Phys. Plasmas **19**, 012704 (2012).

[81] M. J. Rosenberg *et al.*, Phys. Rev. Lett. **120**, 055001 (2018).

[82] A. A. Solodov *et al.*, Phys. Rev. E **106**, 055204 (2022).

[83] S. X. Hu, B. Militzer, V. N. Goncharov, and S. Skupsky, Phys. Rev. Lett. **104**, 235003 (2010).

[84] S. X. Hu, B. Militzer, V. N. Goncharov, and S. Skupsky, Phys. Rev. B **84**, 224109 (2011).

[85] D. I. Mihaylov *et al.*, Phys. Rev. B **104**, 144104 (2021).

[86] Y. H. Ding and S. X. Hu, Phys. Plasmas **24**, 062702 (2017).

[87] S. Zhang *et al.*, Phys. Rev. E **106**, 045207 (2022).

[88] B. I. Bennett, J. D. Johnson, G. I. Kerley, and G. T. Rood, Los Alamos National Laboratory Report No. LA-7130, 1978.

[89] G. P. Schurtz, Ph. D. Nicolaï, and M. Busquet, Phys. Plasmas **7**, 4238 (2000); D. Cao, G. Moses, and J. Delettrez, *ibid.*, **22**, 082308 (2015).

[90] S. X. Hu *et al.*, Phys. Rev. E **90**, 033111 (2014).

[91] See National Technical Information Service Document No. 197808 (W. F. Huebner, A. L. Merts, Magee, N. H., Jr., M. F. Argo, "Astrophysical Opacity Library," Los Alamos National Laboratory, Los Alamos, NM, LA-6760-M, 1977). Copies may be obtained from the National Technical Information Service, Springfield, VA 22161.

[92] R. Epstein, T. J. B. Collins, J. A. Delettrez, S. Skupsky, and R. P. J. Town, Bull. Am. Phys. Soc. **43**, 1666 (1998).

[93] I. V. Igumenshchev *et al.*, Phys. Plasmas **17**, 122708 (2010).

[94] J. A. Marozas *et al.*, Phys. Plasmas **25**, 056314 (2018).

[95] N. Metzler, A. L. Velikovich, A. J. Schmitt, M. Karaski, V. Serlin, A. N. Mostovych, S. P. Obenschain, J. H. Gardner, and Y. Aglitskiy, Phys. Plasmas **10**, 1897 (2003).

[96] V. N. Goncharov, J. P. Knauer, P. W. McKenty, P. B. Radha, T. C. Sangster, S. Skupsky, R. Betti, R. L. McCrory, and D. D. Meyerhofer, Phys. Plasmas **10**, 1906 (2003).

[97] K. Anderson and R. Betti, Phys. Plasmas **11**, 5 (2004).

[98] V. Gopalaswamy *et al.*, Nat. Phys. (to be published).